

RESEARCH

Open Access



Enzymatically responsive nanocarriers targeting PD-1 and TGF- β pathways reverse immunotherapeutic resistance and elicit robust therapeutic efficacy

Ying-Tzu Yen¹, Zhifan Zhang¹, Anni Chen², Yuling Qiu¹, Qin Liu¹, Qin Wang¹, Chunhua Li², Chun Wang¹, Xiaoping Qian¹, Jie Shao¹, Fanyan Meng¹, Lixia Yu^{1,3}, Baorui Liu^{1*} and Rutian Li^{1,3*}

Abstract

Immune checkpoint inhibitors (ICIs) have revolutionized lung cancer treatment, yet resistance remains a challenge. Co-inhibition of PD-1/PD-L1 and TGF- β shows promise but faces limited efficacy and systemic toxicity. We developed gelatinase-responsive nanoparticles (GNPs) delivering anti-PD-1 antibody (α PD-1) and TGF- β receptor I inhibitor galunisertib (Gal). GNPs effectively inhibit tumor progression without observed side effects. Immune profiling by cytometry assay reveals robust recruitment of both activated and exhausted tumor-infiltrating lymphocytes (TILs) and macrophages. Transcriptomic analysis indicates extracellular matrix modulation, supported by reduced collagen deposition and α SMA expression. Fate mapping demonstrates attenuation of Pdgfra⁺ fibroblast transition to α SMA myofibroblasts, potentially reversing “immune-exclusive” status. This study validates GNPs as a promising lung cancer immunotherapy platform, offering mechanistic insights for clinical translation and therapeutic enhancement.

Keywords Transforming growth factor- β , Immune checkpoint inhibitors, Drug resistance, Polymeric nanoparticles, Tumor microenvironment

Introduction

Lung cancer remains a significant contributor to cancer-related mortality, with immunotherapies emerging as promising avenues for treatment. Specifically, immune checkpoint inhibitors (ICIs), such as programmed cell death-1 (PD-1)/programmed cell death ligand-1 (PD-L1) inhibitors, have shown efficacy in reversing immune escape and eliciting antitumor responses. However, resistance to monotherapy poses a challenge, limiting the benefits to only a subset of patients [1]. Transforming growth factor- β (TGF- β), known for its role in immune homeostasis, also plays a crucial role in facilitating immune evasion [2–4] and metastasis [5]. Substantial

*Correspondence:

Baorui Liu
baorui@nju.edu.cn
Rutian Li
rutianli@nju.edu.cn

¹The Comprehensive Cancer Center of Nanjing Drum Tower Hospital, The Affiliated Hospital of Nanjing University Medical School, Nanjing 210008, China

²The Comprehensive Cancer Center of Nanjing Drum Tower Hospital, Clinical College of Nanjing Drum Tower Hospital, Nanjing University of Chinese Medicine, Nanjing 210008, China

³Clinical Cancer Institute of Nanjing University, Nanjing University, Nanjing 210008, China



© The Author(s) 2025. **Open Access** This article is licensed under a Creative Commons Attribution-NonCommercial-NoDerivatives 4.0 International License, which permits any non-commercial use, sharing, distribution and reproduction in any medium or format, as long as you give appropriate credit to the original author(s) and the source, provide a link to the Creative Commons licence, and indicate if you modified the licensed material. You do not have permission under this licence to share adapted material derived from this article or parts of it. The images or other third party material in this article are included in the article's Creative Commons licence, unless indicated otherwise in a credit line to the material. If material is not included in the article's Creative Commons licence and your intended use is not permitted by statutory regulation or exceeds the permitted use, you will need to obtain permission directly from the copyright holder. To view a copy of this licence, visit <http://creativecommons.org/licenses/by-nc-nd/4.0/>.

studies suggest that concurrent targeting of PD-1/PD-L1 and TGF- β pathways could enhance antitumor efficacy by overcoming immune checkpoint protein binding and improving cytotoxic T lymphocyte (CTL) infiltration [6–10]. Despite the potential advantages, challenges such as limited drug penetration and systemic side effects hinder the clinical application of this combinative strategy [11, 12].

Previously, we described gelatinase-stimulated nanoparticles composed of methoxy poly (ethylene glycol) (mPEG), gelatinase-cleavable peptide Pro-Val-Gly-Leu-Iso-Gly (PVGLIG), and poly (ϵ -caprolactone) (PCL) (mPEG-PVGLIG-PCL). This nanoparticle system allows for targeted drug delivery and prolonged retention at gelatinase-rich tumor sites, potentially reducing nonspecific release and associated side effects [13]. Further, the

core-shell structure allows for the simultaneous loading and delivery of both hydrophobic and hydrophilic drugs, facilitating a synergistic effect. In this study, by incorporating both α PD-1 antibody (α PD-1) and TGF- β receptor 1 inhibitor galunisertib (Gal, LY2157299) onto these nanoparticles (referred to as GPNPs), we aim to address both immunotherapeutic resistance and treatment-related side effects.

Using a lung cancer syngeneic murine model with poor immunogenicity [14, 15], we hypothesize that GPNPs can disrupt the collagenous extracellular matrix (ECM) barrier and improve immunotherapeutic efficacy. We profile immune- and ECM-associated transcriptomic signatures using cytometry-based techniques and RNA sequencing, respectively, to elucidate the mechanisms underlying these effects. Additionally, we trace the lineage and fate

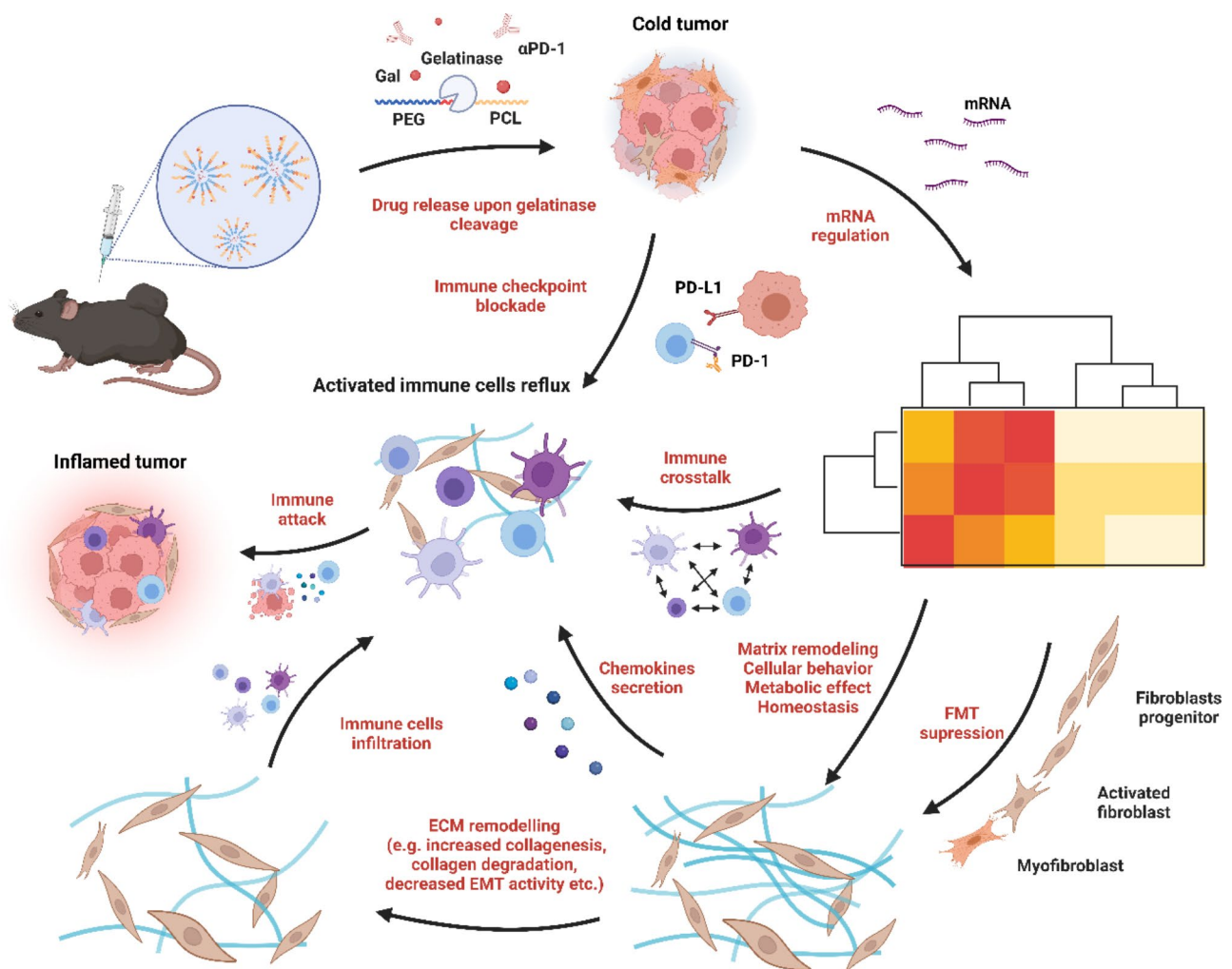


Fig. 1 Schematic illustration of systemic α PD-1/Gal-loaded gelatinase-responsive nanoparticle (GPNP) injection to enhance tumor immunotherapy through modulation of the tumor microenvironment. GPNPs, consisting of α PD-1, Gal, and gelatinase-responsive nanoparticles, were administered systemically. Upon arrival at gelatinase-rich tumor microenvironments, GPNPs underwent enzymatic degradation, leading to activated immune cell reflux and transcriptomic alterations, including extracellular matrix (ECM) remodeling, epithelial-to-mesenchymal transition (EMT), suppression of fibroblast-to-myofibroblast transition (FMT), and modulation of immune crosstalk

of fibroblasts, the main contributors to ECM and collagen production, using a transgenic murine model (Fig. 1).

This study aims to contribute insights into the advancement of gelatinase-responsive nanoparticle-based drug delivery strategies, with the objective of overcoming immunotherapeutic resistance and augmenting treatment outcomes in lung cancer.

Results

Fabrication and characterization of GPNPs

Methoxy-PEG-PVGLIG-PCL was synthesized through an amidation reaction (Fig. 2A and Fig. S1A). GPNPs were then formulated by loading α PD-1 and Gal onto mPEG-PVGLIG-PCL using the double emulsion method (Fig. 2A). Transmission electron microscopy (TEM)

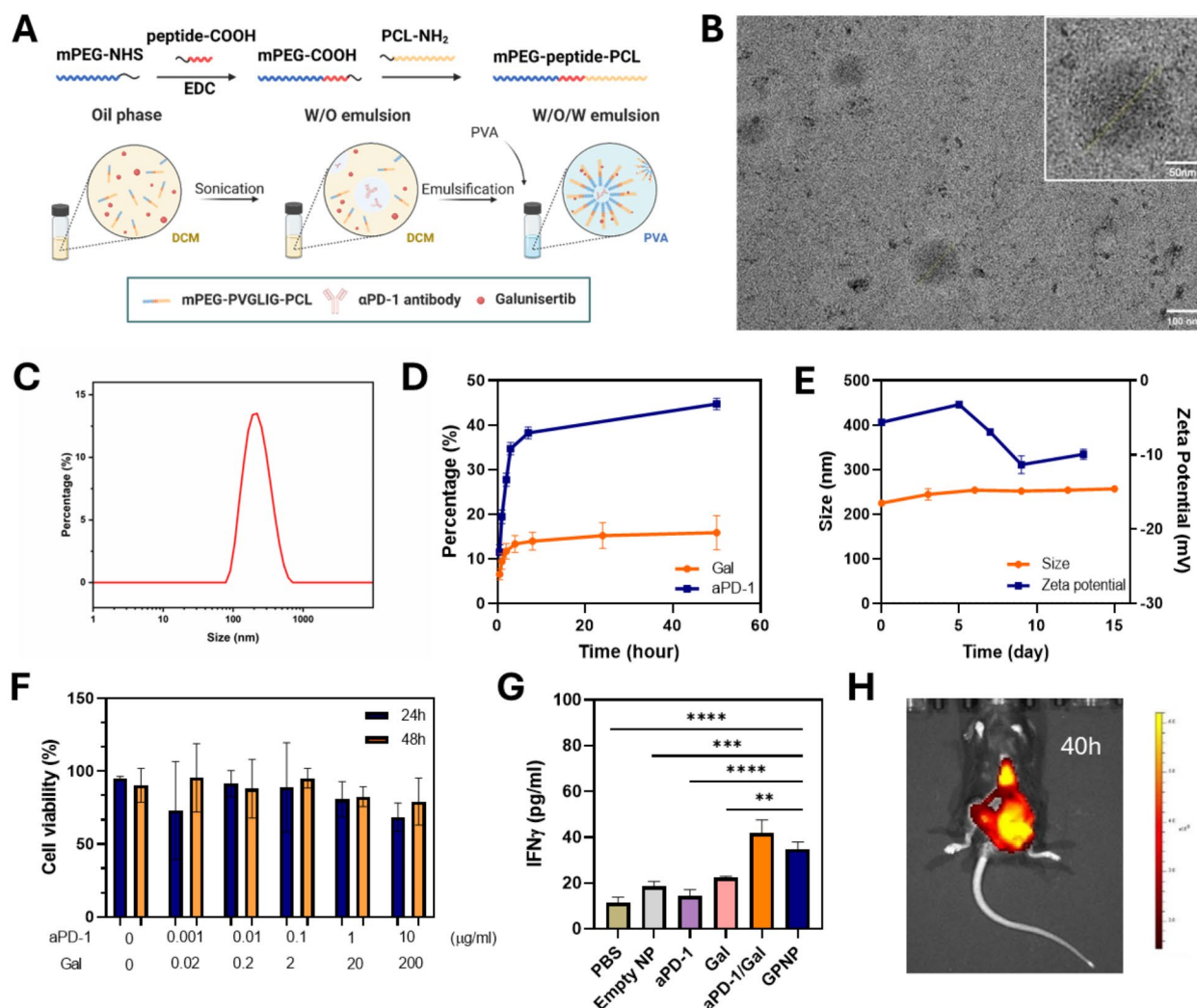


Fig. 2 Fabrication and characterization of Gelatinase-Responsive Nanoparticles (GPNPs). **(A)** Schematic illustration of GNP preparation. **(B)** Transmission electron microscopy (TEM) image showing the round-shape morphology of GPNPs. **(C)** Size histogram of the size distribution of GPNPs measured by dynamic light scattering (DLS). **(D)** In vitro drug release profiles of GPNPs. **(E)** Stability assessment of GPNPs over time, measured by changes in sizes and zeta potentials using DLS method. **(F)** Cell viability assay conducted on Lewis lung carcinoma (LLC) cells after incubation with different formulations of GPNPs for 24–48 h. **(G)** Quantification of interferon-gamma (IFN γ) secretion in drug-containing medium from a co-incubation system of cytokine-induced killer (CIK) and H1299 cells (at a ratio of 10:1). **(H)** In vivo targeting capability evaluation of nanoparticles carrying DiR near-infrared dye. PBS, phosphate buffer saline; α PD-1, anti-PD-1 antibody; Gal, TGF- β receptor I inhibitor galunisertib; GNP, gelatinase-responsive nanoparticles

revealed the spherical morphology of GPNPs (Fig. 2B). GPNPs exhibited a neutral surface charge (0.1136 ± 0.158) and hydrodynamic diameters of 224.67 ± 2.40 nm, with a low polydispersity index (0.29 ± 0.04) (Fig. 2C). The loading capacity of α PD-1 and Gal was $11.37 \pm 0.30\%$ and $4.32 \pm 0.11\%$, respectively, with corresponding encapsulation efficiencies of $75.68 \pm 1.04\%$ and $47.50 \pm 0.12\%$. Over 40% of α PD-1 and 15% of Gal in GPNPs were released within 50 h (Fig. 2D). No significant changes in sizes and zeta potentials were observed over time, indicating the stability of GPNPs (Fig. 2E and Fig. S1B). Cell viability and IFN γ secretion assays demonstrated that GPNPs with different formulations exhibited minimal cytotoxicity (Fig. 2F) but enhanced immune function (Fig. 2G). Interestingly, the killing assay showed no superior efficacy at a ratio of 20:1 in the α PD-1/Gal group compared to the GNP group (Fig. S1C, D). The targeting capability of the carrier was confirmed by the aggregation of DiR-loaded nanoparticles at tumor sites within 40 h (Fig. 2H and Fig. S1E).

Antitumor efficacy and toxicity evaluation of GPNPs

Subsequently, we evaluated the antitumor efficacy of GPNPs in a subcutaneous Lewis lung carcinoma (LLC) murine model. Mice were treated when the tumor volume reached approximately 100 mm^3 (Fig. 3A). GPNPs were administered once a week for a total of two doses. Tumors in mice treated with saline and α PD-1 exhibited aggressive growth. GPNPs induced substantial inhibition of tumor growth, while a modest delay in tumor growth was observed in mice treated with α PD-1/Gal (Fig. 3B–D). Moreover, 60% of the treated mice survived 18 days after the initiation of GPNPs treatment, whereas α PD-1/Gal treatment conferred minimal survival benefits (Fig. 3E). In an A549-harboring BALB/c nude mice model (Fig. S2A), with combination of CIK cells (Fig. S2B), the GNP-treated group showed delayed tumor growth (Fig. S2C) and prolonged survival (Fig. S2D), suggesting immune-boosting capabilities. Given the critical role of long-term immune memory in determining immunotherapeutic efficacy, we conducted a reseeding assay using the LLC murine model. A decrease in tumorigenesis incidence and a reduction in tumor growth rate in mice previously treated with GPNPs were observed (Table S1 and Fig. S3).

During the treatment, we monitored the body weights of mice, and no significant weight changes were observed (Fig. 3F). At the end of the regimens, major organ specimens were excised from the mice and stained with hematoxylin and eosin (H&E, Fig. S4A), revealing no discernible histological alterations. Moreover, no significant differences in serum biomarkers related to cardiac (Fig. S4B), liver (Fig. S4C), and renal (Fig. S4D) function were detected among the groups. However, a slight increase

in cardiac biomarkers was observed in the α PD-1 group (Fig. S4B), indicating a potential heightened risk of cardiac disease induction.

These findings collectively indicate that the administration of GPNPs effectively enhanced the anti-tumor response and promoted the development of long-term immunity.

Immune signatures in TME

Given the demonstrated capability of GPNPs to exhibit prominent antitumor efficacy *in vivo*, the context of tumor heterogeneity remained poorly understood. Hence, we investigated the immunophenotyping signatures using flow cytometry to elucidate the landscape of the tumor microenvironment (TME, Table S2). Both GPNPs ($p=0.0051$) and α PD-1/Gal ($p=0.0151$) treatments facilitated the infiltration of CD8 $^+$ T cells compared to the control (Fig. S5A). GPNPs treatment increased the ratio of both early activated CD38 $^+$ CD8 $^+$ (Fig. 4A) and CD69 $^+$ CD8 $^+$ (Fig. S5B) T cells relative to α PD-1/Gal ($p=0.0136$, $p=0.2537$), α PD-1 ($p=0.0106$, $p=0.0127$), or the control ($p=0.0113$, $p=0.0295$). Interestingly, GPNPs treatment also increased the ratio of dysfunctional T cells, PD-1 $^+$ CD8 $^+$ T cells, relative to α PD-1/Gal ($p=0.0126$), α PD-1 ($p=0.0155$), or the control ($p=0.0256$) (Fig. 4B).

In addition to its effects on CD8 $^+$ T cells, GNP treatment increased the infiltration of CD4 $^+$ T cells relative to α PD-1/Gal ($p=0.0083$), α PD-1 ($p=0.0165$) or the control ($p=0.0114$) (Fig. 4C). GPNPs treatment increased the ratio of immunosuppressive Treg ($p=0.0215$) (Fig. 4D) and PD-1 $^+$ Treg ($p=0.0112$) (Fig. S5C) compared to the control ($p=0.0215$ and $p=0.0112$, respectively) and to α PD-1 ($p=0.0311$ and $p=0.0137$, respectively). However, activated CD69 $^+$ Treg increased after GPNPs treatment compared to the control ($p=0.032$) (Fig. S5D).

Aside from lymphoid cells, GPNPs treatment affected monocyte/macrophage (Mo/Mf) populations. α PD-1/Gal treatment decreased type I macrophages (M1) relative to α PD-1 ($p=0.0033$) and the control ($p=0.0086$) (Fig. S5E). GPNPs treatment decreased the ratio of type II macrophages (M2) relative to α PD-1 ($p=0.0006$) (Fig. 4E). As a measurement for evaluating the dominant role of macrophages, higher M1/M2 ratio was discovered in α PD-1 group when compared with α PD-1/Gal ($p=0.0007$) and the control ($p=0.0305$). (Fig. S5F). Although GNP group did not obtain a better M1/M2 ratio compared to the control, it showed a superior M1/M2 ratio when compared with α PD-1/Gal group with higher pro-inflammatory M1 ratio and lower anti-inflammatory M2 ratio.

To comprehensively understand the immune composition, we simultaneously screened a total of 41 immune-associated markers by using cyTOF. More than 37

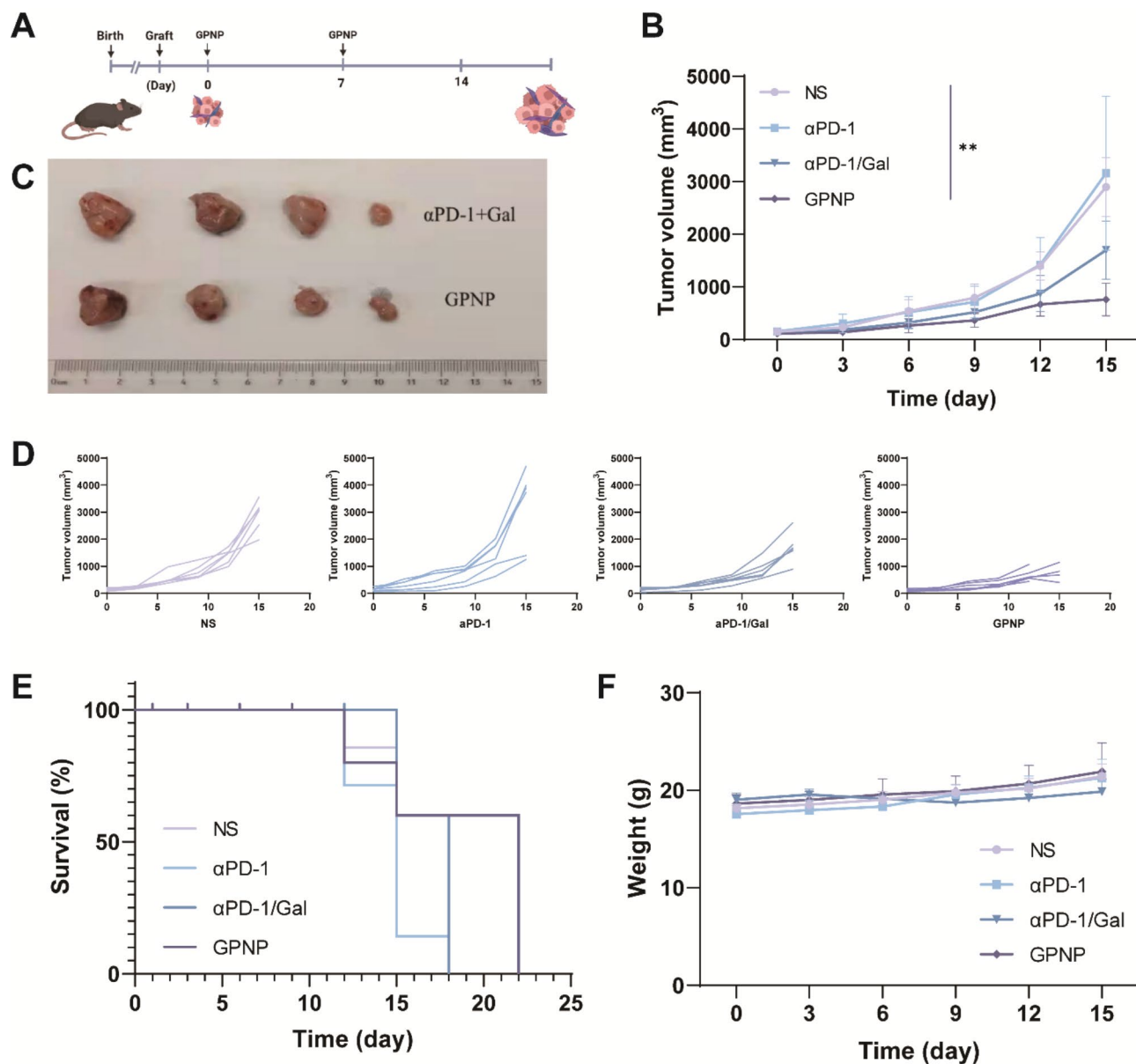


Fig. 3 In vivo therapeutic efficacy of gelatinase-responsive nanoparticles (GNPs) in the Lewis lung carcinoma (LLC) model. **(A)** Treatment regimen: C57BL/6 mice were subcutaneously implanted with LLC cells (2×10^6) and intraperitoneally administered with different formulations once the tumor reached $\sim 100 \text{ mm}^3$. The weekly dosages of $\alpha\text{PD-1}$ and Gal were 10 mg/kg and 150 mg/kg , respectively. In the $\alpha\text{PD-1}/\text{Gal}$ group, Gal was administered three times a week. GNP and saline were administered once a week. **(B)** Tumor growth curves following different treatment ($n=6$ per group). **(C)** Tumor specimens of group $\alpha\text{PD-1}/\text{Gal}$ and group GNP at the end of the regimens in the Lewis lung carcinoma (LLC) model. **(D)** Individual tumor volume changes in each mouse across different treatment groups ($n=6$ per group). **(E)** Kaplan-Meier curves for survival of mice ($n=6$ per group). **(F)** Body weight changes with different regimens ($n=6$ per group). NS, normal saline; $\alpha\text{PD-1}$, anti-PD-1 antibody; $\alpha\text{PD-1}/\text{Gal}$, anti-PD-1 antibody and TGF- β receptor I inhibitor galunisertib; GNP, gelatinase-responsive nanoparticles

clusters were identified (Table S3) and could be characterized as Mo/Mf, T cells, B cells, dendritic cells (DCs), myeloid-derived suppressor cells (MDSCs) and their subtypes (Fig. 4F). In general, Mo/Mf occupied the majority of the immune infiltration population (Fig. S6A). Compared to other regimens, GNP treatment demonstrated a distinct phenotypic T cell profile within the tumor, characterized by the highest proportion of CD8^+ T cells

and the lowest percentage of CD4^+ regulatory T cells (Fig. 4G and Fig. S6B). In Mo/Mf, $\text{PD-L1}^+\text{CD38}^+\text{CD206}^+$ M2 macrophages and $\text{PD-1}^+\text{CD38}^+\text{MHCII}^{\text{low}}\text{CD206}^+$ M2 macrophages were nearly absent in GNP group.

Consistent with our results obtained by flow cytometry, the tumor after GNP treatment showed an increase in activated CD8^+ T cells (Fig. 4H) and total T cells (Fig. 4I), including $\text{Ly6C}^+\text{CD38}^+\text{CD69}^+\text{PD-1}^+\text{CD8}^+$ T

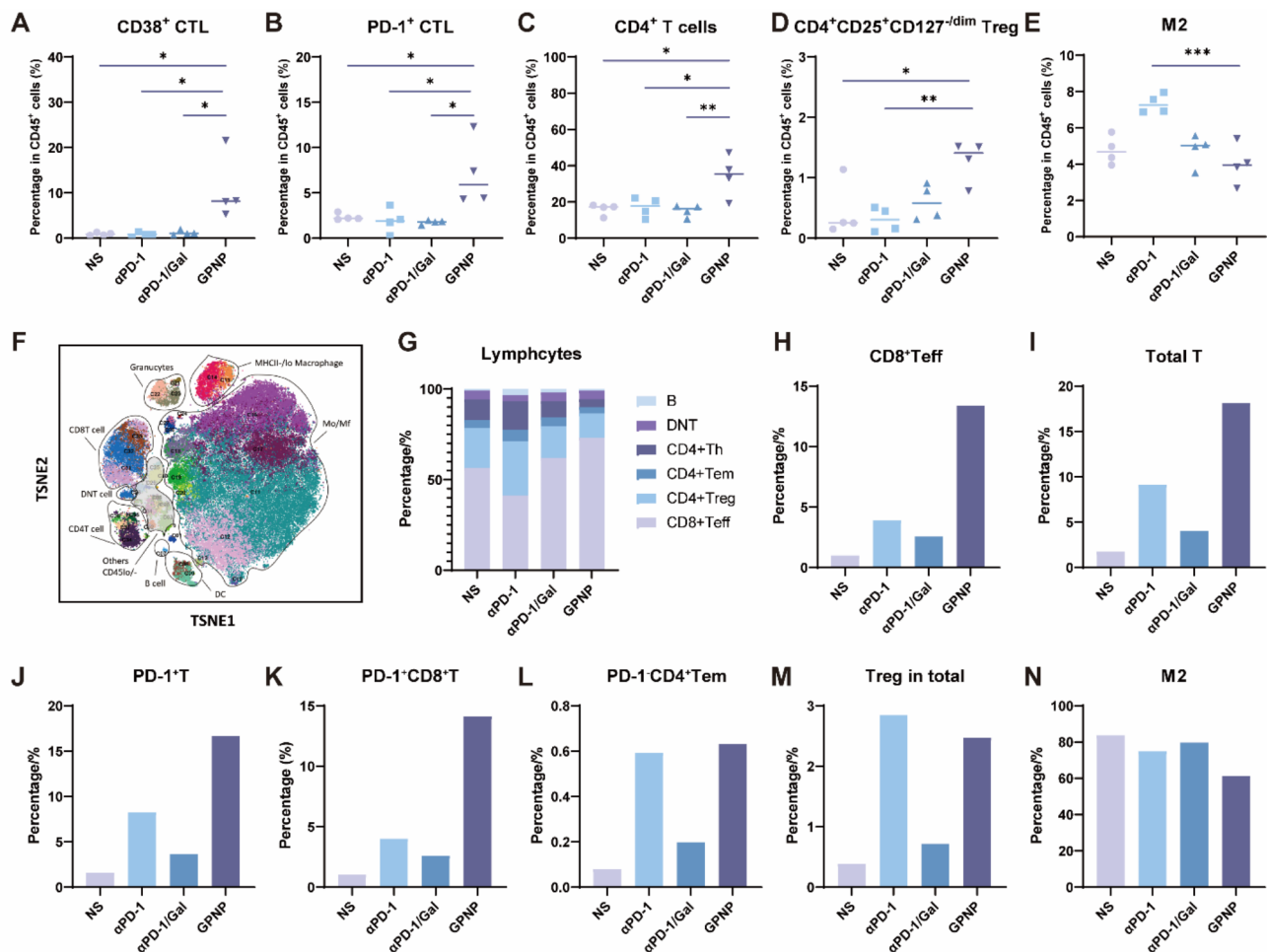


Fig. 4 GPNPs elicit distinct immune profile in LLC tumor-bearing mice. Flow cytometry results of (A) CD38⁺ Cytotoxic T lymphocytes (CTLs), (B) PD-1⁺CTLs, (C) CD4⁺ T cells, (D) CD25⁺CD127^{-dim} Treg cells, (E) M2 in TME after different treatments. (F), tSNE plot showing cell clusters with corresponding identity, (G) Histogram displaying cell proportion of T cells in each group. Proportion of (H) CD8⁺Teff, (I) total T cells, (J) PD-1⁺T cells, (K) PD-1⁺CD8⁺T cells, (L) PD-1⁻CD4⁺ Tem, (M) Treg, and (N) M2 per group according to cyTOF. CTLs, Cytotoxic T lymphocytes; Treg, regulatory T cells; M2, alternatively activated macrophages; Teff, effector T cells; Tem, effective memory T cell; NS, normal saline; α PD-1, anti-PD-1 antibody; α PD-1/Gal, anti-PD-1 antibody and TGF- β receptor I inhibitor galunisertib; GPNP, gelatinase-responsive nanoparticles; ns, not significant, $p > 0.05$, * $p < 0.05$, ** $p < 0.01$, *** $p < 0.001$

cells. In addition, the results of cyTOF showed that the expression of PD-1⁺ in T cells (Fig. 4J) and CD8⁺T cells (Fig. 4K) in the GPNP group was significantly higher than that in the other groups, which was also consistent with our flow cytometry results. It is worth mentioning that we also found a population of PD-1⁻CD4⁺ memory T cells (Fig. 4L), which were highly expressed in the GPNP group, suggesting that CD4⁺ T cells may play a major role in the effect of GPNP treatment on immune memory. The proportions of Treg cells (Fig. 4M) and M2 cells (Fig. 4N) showed a similar trend in cyTOF and flow cytometry results.

In general, the disparities between groups mainly focused on M1, M2 and CD8⁺ T cells, especially when integrated with functional markers, including activation (CD38, CD69), immune checkpoint (PD-1, PD-L1).

Further, we performed bulk mRNA sequencing (RNA-seq) to evaluate transcriptomic differences of TME between tumors treated with and without nanoparticles. When analyzing the differential gene expression between the α PD-1/Gal and GPNP groups, we excluded the GPNP-3 data to mitigate the aberrant pattern observed in the GPNP group (Fig. S7A). Comparing α PD-1/Gal group with GPNP group, two up-regulated genes (*Ccl21d*, *Atn1*) and 40 down-regulated genes were uncovered ($|\log_2\text{Fc}| > 1$, FDR < 0.05) (Fig. S7B). Among these genes, α PD-1/Gal up-regulated *Ccl21d*, while *Slc7a2*, *Cxcl5*, *Il1rn*, *Cxcl2*, *Cxcl12*, and *Ccl11* were preferably up-regulated in GPNP group. *Sfrp2*, *Slc7a2*, *Cdh11* and *Fbln7*, which involved in macrophage reprogramming, were also differential expressed (Fig. 5A, B).

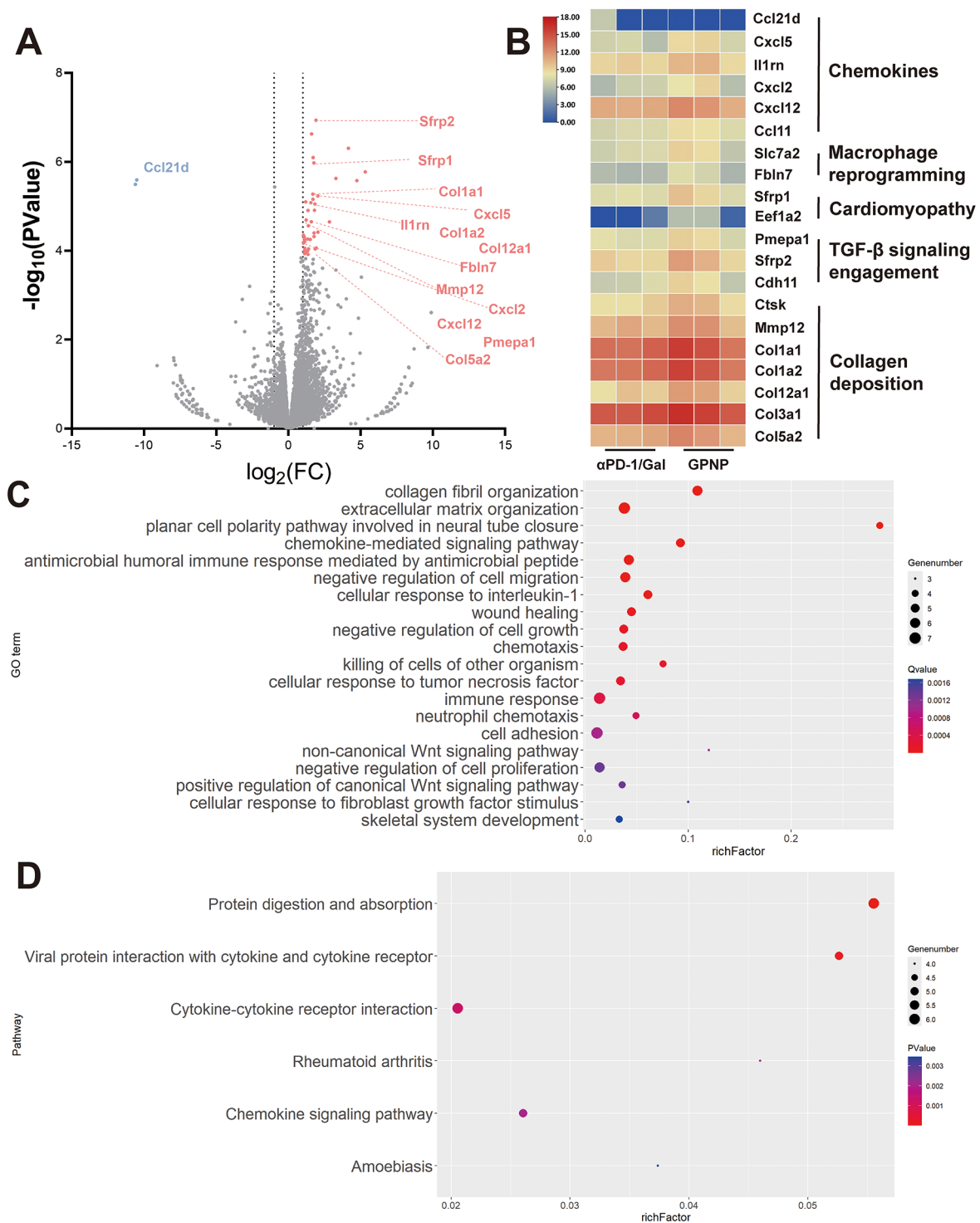


Fig. 5 RNAseq analysis of αPD-1/Gal vs. GPNP treatment. **(A)** The volcano map of differentially expressed genes. The red dots of significant genes were up-regulated and the blue dots were down-regulated. **(B)** Heatmap of genes related to chemokines, macrophage reprogramming, cardiomyopathy, TGF-β signaling engagement and collagen deposition. **(C)** Go enrichment histogram. The abscissa is the percentage of genes and the ordinate is the corresponding enriched GO terms. **(D)** Scatter plot of KEGG enrichment. The vertical axis represents the name of the pathway, and the horizontal axis represents the rich factor. The size of the dots indicates the number of differentially expressed genes in the pathway, and the color of the dots corresponds to different P value ranges. αPD-1/Gal, anti-PD-1 antibody and TGF-β receptor I inhibitor galunisertib; GPNP, gelatinase-responsive nanoparticles

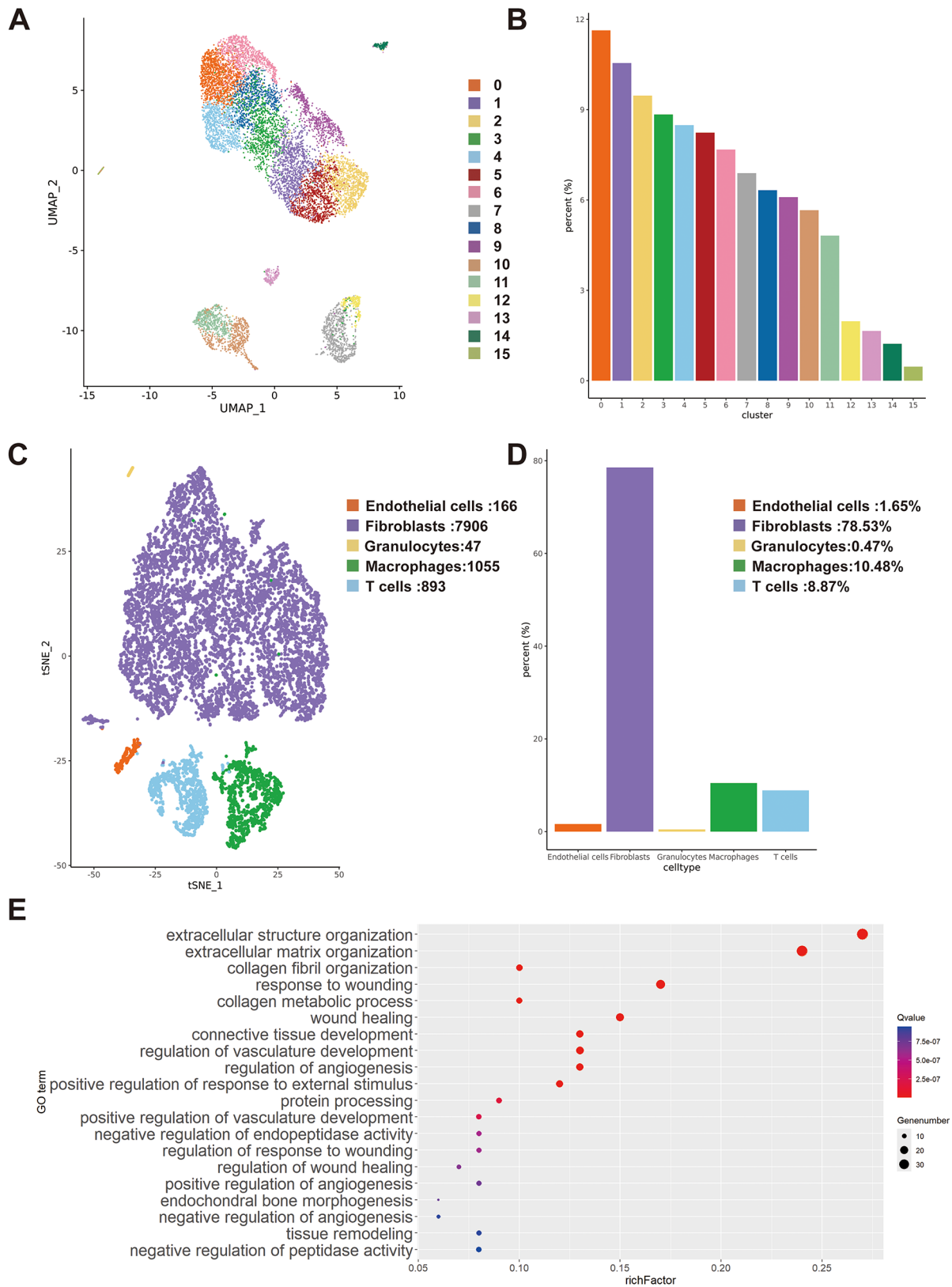


Fig. 6 (See legend on next page.)

(See figure on previous page.)

Fig. 6 scRNAseq analysis of GPNP-treated tumor. (*n* = 1) **(A)** Percentage of 16 clusters identified by Seurat package. **(B)** Percentage of 16 clusters. **(C)** tSNE of 5 major cell types (fibroblast, macrophage, T cell, endothelial cell and granulocyte) based on SingleR package. **(D)** Percentage of 5 major cell types, including fibroblasts (78.53%), macrophages (10.48%), T cells (8.87%), endothelial cells (1.65%) and granulocytes (0.47%). **(E)** Scatter plot of cluster 14 GO enrichment regarding matrix remodeling. NS, normal saline; α PD-1, anti-PD-1 antibody; α PD-1/Gal, anti-PD-1 antibody and TGF- β receptor I inhibitor galunisertib; GPNP, gelatinase-responsive nanoparticles

ECM modification in TME

By conducting bulk RNAseq analysis, we observed that GPNP treatment exerted a discernible impact on ECM remodeling. Specifically, genes associated with collagen deposition, including *Col1a1*, *Col1a2*, *Col12a1*, *Col3a1* and *Col5a2*, were significantly up-regulated in the GPNP group (Fig. 5B). Additionally, there were notable differences in the expression of genes related to the TGF- β signaling pathway (*Pmepa1*, *Sfrp2* and *Cdh11*) as well as cardiomyopathy-related genes (*Sfrp21* and *Eef1a2*), when compared to the control group receiving only the drug (Fig. 5B).

Gene Ontology (GO) enrichment revealed that the 42 genes were significantly associated with chemotaxis, immune response, cell adhesion, negative regulation of cell growth, extracellular matrix organization, collagen fibril organization, negative regulation of cell growth, negative regulation of cell migration, neutrophil chemotaxis, non-canonical Wnt signaling pathway, cellular response to fibroblast growth factor stimulus, chemokine-mediated signaling pathway, cellular response to IL-1, cellular response to tumor necrosis factor and positive regulation of canonical Wnt signaling pathway (Fig. 5C). Kyoto Encyclopedia of Genes and Genomes (KEGG) enrichment showed that 5 pathways were involved, including chemokine signaling pathway, protein digestion and absorption, and cytokine-cytokine receptor interaction (Fig. 5D).

To our best knowledge from the above findings, the synergy effect of α PD-1 and Gal were more likely to be correlated to the degradation of extratumoral collagen. Therefore, we decided to further investigate through single-cell RNA sequencing (scRNAseq) and fate mapping model in an attempt to rationalize the chaos of ECM in TME.

Single-cell transcriptomes of a GPNP-treated tumor were obtained from a total 10,726 cells with mean 33,559 reads/cell and median 2,939 genes/cell. Unbiased clustering of cells identified 16 main clusters and could be categorized into 5 major cell types, including cancer-associated fibroblasts (CAF, 78.53%), tumor-associated macrophages (TAM, 10.48%), T cells (8.87%), endothelial cells (1.65%) and granulocytes (0.47%) (Fig. 6A-D) [16]. Marker genes were identified and displayed by clusters (Fig. S8). To better understand the heterogeneity of each cell type, regarding the lack of general consensus on the definite classification [17], manual annotation was performed based on the expression of specific

cellular markers. Cells in cluster 0 expressed high levels of *Tm4sf1*, *Fosb*, *Hspb8*, *Bag3*, *Dnajb1*, *Dnajb4*, *Errfi1* and *Serpine 1* were identified as migratory CAF. Cluster 2 was classified as proliferative CAF since the broad expression of proliferation-associated genes (*Ube2c*, *Birc5*, *Ccna2*, *Cnb1*, *Ccnb2*, *Cdc20*, *Cenpa*, *Tpx2*, *Racgap1*, *Hmmr*, *Plk1*, *Cenpe*, *Cenpf*, *Prc1*, *Top2a*, *Anln*, *Cks1b*, *H1f0*). With high expression of Cd274 (alias PD-L1) and IFN-related genes (*Igtp*, *Gbp2*, *Ifit3*, *Ifit1*, *Iigp1*, *Irgm1*, *Isg15*, *Ifit2*), cluster 4 was categorized as immunomodulatory CAF. While high-expression genes in cluster 5 were mostly involved in nucleic acid metabolism (*Pclaf*, *Rrm2*, *Tk1*), cluster 6 engaged more in proteolysis activity (*Igfbp4*, *Cfh*, *Fn1*). Cluster 14, in particular, highly expressed collagen gene family (*Col1a2*, *Col5a2*, *Col6a2*, *Col15a1*, *Col14a1*, *Col12a1*, *Col6a3*, *Col1a1*, *Col3a1*, *Col6a1*, *Col5a3*, *Col5a1*, *Col4a2*) and other ECM-modifying genes (*Dcn*, *Fbln2*, *Lox*, *Postn*, *Serpina3n*, *Mfap5*, *Sod3*, *Timp3*, *Thbs4*, *Adamts2*, *Ctsk*, *Osmr*, *Serpine2*, *Cygb*, *Abi3bp*, *Cilp*, *Antxr1*, *Colec12*, *Mrc2*, *Loxl2*, *Dpt*, *Spon1*, *Lum*, *Inhba*, *Loxl1*, *Igfbp7*, *Ltbp2*, *Fn1*, *Serpinb2*, *Bmp1*, *Nid1*, *Spp1*) and was therefore designated as matrix remodeling CAF. Of note, no significant myofibroblast-related gene expression (i.e. *Acta2*) was observed in GPNP-treated tumor. Cluster 7, cluster 10, cluster 11, cluster 12, cluster 13 and cluster 15 were defined as CD4 T cells (*Cd28*, *Cd3d*, *Cd3e*, *Cd3g*, *Cd4*, *Cd69*, *Ctla4*, *Icos*, *Pdcd1*, *Tnfrsf9*), M1 (*Cd68*, *Fcgr3*, *Msr1*, *Cd14*), M2 (*Csf1r*, *Mec1*, *Msr1*), CD8 T cells (*Cd28*, *Cd3d*, *Cd3e*, *Cd3g*, *Cd8a*), endothelial cells (*Pcam1*, *Cdh5*, *Kdr*, *Tspaan7*, *Edn1*) and granulocytes (*Itgam*, *Cd80*, *Fcgr3*), respectively, with their unique gene signatures.

Among all clusters, cluster 14 revealed particular signatures in accordance with bulk sequencing results (*Col1a2*, *Col5a2*, *Cxcl12*, *Cxcl5*, *Postn*, *Sfrp2*, *Gas1*, *Ccl11*, *Ctsk*, *Serpine2*, *Cyp1b1*, *Sfrp1*, *Col12a1*, *Bgn*, *Pmepa1*, *Saa3*, *Col1a1*, *Spon1*, *Col3a1*) and was further analyzed to explore its potential role in GPNP-treated tumor. The GO enrichment analysis showed upregulated genes in ECM remodeling cluster enriched in 13 cellular components, 44 molecular functions and 385 biological processes. Cellular components of upregulated genes mainly located at collagen-containing ECM, basement membrane and secretory granule (Fig. S9A). Molecular functions, on the other hand, focused on ECM binding, PDGF binding, chemokine binding, proteoglycan binding, cell adhesion molecule binding, Smad binding, oxidoreductase activity and metalloproteinase (Fig. S9B). Enriched biological

processes included matrix remodeling (collagen deposition, proteolysis, protein phosphorylation) (Fig. 6E), immune crosstalk (chemokine, leukocyte, monocyte/macrophage, complement) (Fig. S10), cellular behavior (cell growth, proliferation, apoptosis, secretion, adhesion, motility) (Fig. S11), metabolic effects (oxygen, hormone, retinoid, lipid), homeostasis (coagulation) and signaling crosstalks (TGF- β pathway, BMP pathway, Wnt pathway) (Fig. S12). KEGG enrichment analysis showed connection with ECM-receptor interaction, protein digestion and absorption, cytokine-cytokine receptor interaction, complement and coagulation cascades, focal adhesion, proteoglycans in cancer, phagosome, IL-17 signaling, chemokine signaling, TNF signaling, relaxin signaling and TGF- β signaling pathways (Fig. S13). Similar to the results from GO enrichment assay, Reactome enrichment analysis displayed correlations with ECM organization, PDGF signaling, cell motility, regulation of insulin-like growth factor (IGF) transport and uptake by IGF binding proteins (IGFBPs), complement cascade, IL-6 signaling, chemokine, o-glycosylation, laminin interaction, coagulation, eNOS activation, and lipoprotein regulation. (Fig. S14).

Contribution of fibroblasts in collagen deposition and fibroblast fate mapping

To verify the alterations in ECM indicated by transcriptomic assays, we performed Masson's trichrome analysis of tumor tissues and observed high level of collagen deposition, especially perivascular area, in the control group while α PD-1/Gal and GPNPs groups were stained almost negative (Fig. 7A). The phenomenon confirmed the ECM remodeling transcriptomic alterations in RNA sequencings. Thus, we hypothesized that the collagen barrier confined the infiltration of immune cells and brought about the discrepancy between the efficacy of different treatments.

Fibroblasts were the major component in extracellular matrix and, to a great extent, contributed to collagen formation once activated [18]. In light of the hints from Masson's trichrome staining and RNA sequencing, we sought to explore the underlying mechanism of collagen-associated transformation induced by fibroblasts after therapeutic interventions. To understand the extent of fibroblast-to-myofibroblast transition, we performed immunohistochemistry and observed overwhelming expression of α SMA, a myofibroblast-specific marker, in the control group in comparison with GPNP group (Fig. 7B).

Moreover, we selected *Pdgfra* as the target regarding its implication as progenitors in fibroblast lineage and the results from RNAseq. To disclose the lineage potency, we established a *Pdgfra-Cre; Rosa26-CAG-LSL-tdTomato* (*Pdgfra-Cre/TdT*) transgenic murine model for

fate mapping assay, where *Pdgfra*⁺ cells could be traced by permanent tdTomato fluorescence driven by Cre recombinase transcription (Fig. 7C). The model was further validated by genotypic assay and fluorescence examination (Table S5 and Fig. S15 A-D). At day 14 from tumor formation, we discovered co-localization of *pdgfra* and α SMA in NS and α PD-1 groups (Fig. 7D), confirming the existence of fibroblast activation and fibroblast-to-myofibroblast transition (FMT) activity in TME. Conversely, we did not observe *pdgfra*- α SMA co-expression in neither α PD-1/Gal- nor GPNP-treated group (Fig. 7D), suggesting that both of the treatments could stabilize fibroblasts by similar mechanism and the difference was too subtle that could only be revealed in transcriptomic level as evidenced by our RNA sequencing results. Interestingly, co-localization of *pdgfra* and vimentin existed in α PD-1/Gal group but not in GPNP group (Fig. 7D). Besides, *pdgfra* co-localization with laminin and fibronectin were observed, respectively, in α PD-1 group (Fig. 7D).

Discussion

Our study developed a biocompatible gelatinase responsive nanocarrier loaded with α PD-1 and TGF- β receptor I inhibitor. The nanoscale delivery system was able to effectively target tumor without apparent systemic loss. Prominent antitumor efficacy, long term memory and safety profile were demonstrated in immunologically "cold" LLC syngeneic murine model [14] and A549 murine model. Applying GPNPs in lung cancer treatment allowed remodeling of TME (both immune system and ECM), arousing potent anti-tumor immune response and creating an immune-permissive environment (Fig. S16).

To interrogate the immune profile within TME subjected to GPNP treatment, we employed the analysis of flow cytometry and cyTOF. From the results, GPNPs treatment increased the ratio of both early activated CD38⁺CD8⁺ (Fig. 4A) and CD69⁺CD8⁺ T cells (Fig. S5B), suggesting a higher proportion of activated cells mediating cytotoxic activity, potentially contributing to the superior efficacy of GPNP treatment. In addition, there is an increased ratio of PD-1⁺CD8⁺ T cells (Fig. 4B, K) after GPNP treatment. PD-1 expression on CD8⁺ T cells is often associated with dysfunction and results in an exhausted signature within the tumor microenvironment. However, PD-1⁺CD8⁺ T cells have also been reported to exhibit equivalent functionality to PD-1⁻CD8⁺ T cells [19]. Therefore, the role of PD-1⁺CD8⁺ T cells as either proponents or suppressors of antitumor activity warrants further investigation. The up-regulation of the CD4⁺ T cell proportion (Fig. 4C) simultaneously presents a perplexing aspect, as it leads to an increase in both CD4⁺ T helper cells that promote antitumor responses and CD4⁺ Treg cells (Fig. 4D) with immunosuppressive

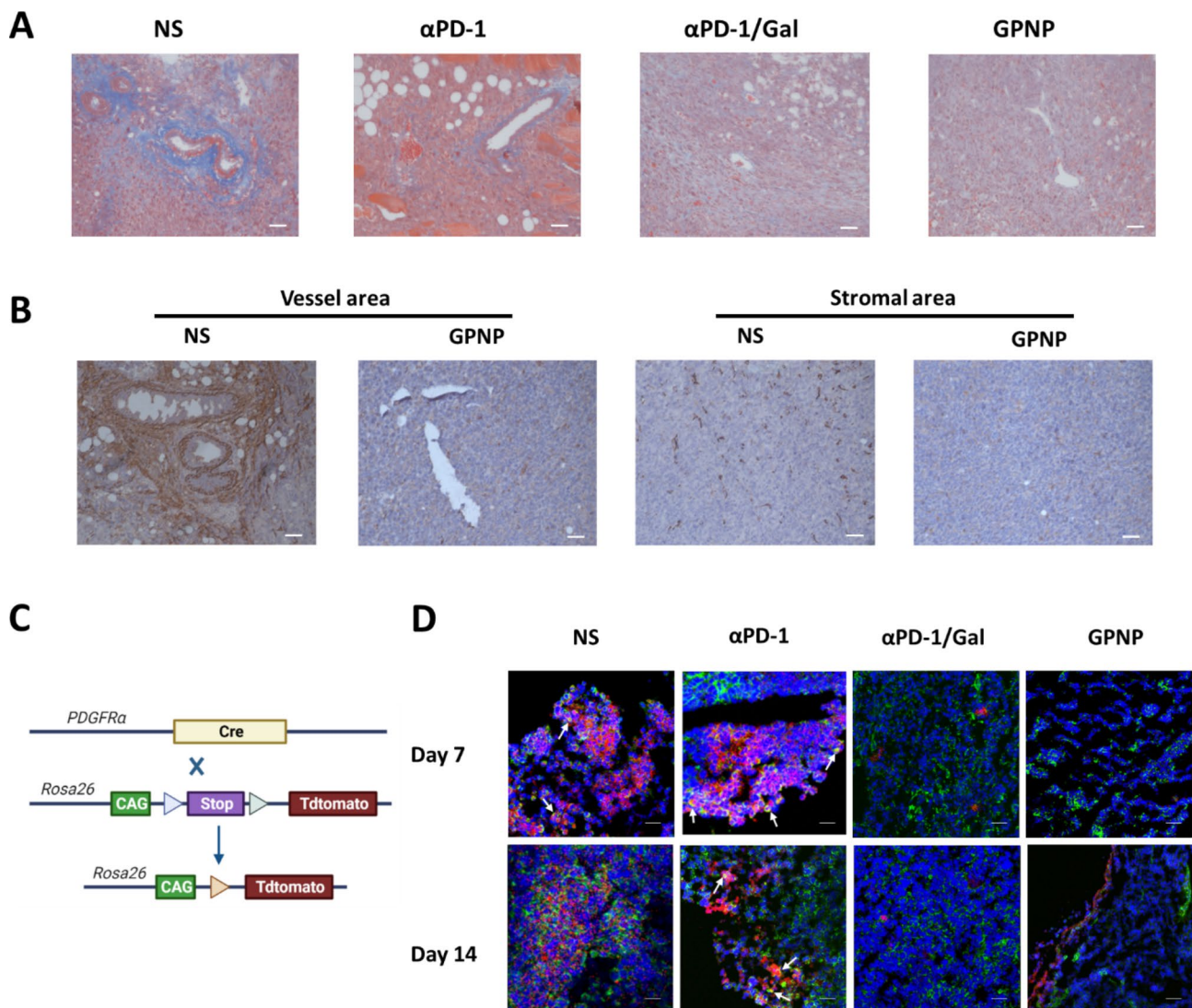


Fig. 7 Collagen deposition and fate mapping of *Pdgfra*⁺ cells. **(A)** Collagen deposition of each treatment. (blue: collagen) **(B)** αSMA staining in NS and GPNP group. **(C)** Gene background of *Pdgfra*-tracing murine model. **(D)** Co-localization of *pdgfra* and fibroblast markers (αSMA, vimentin, laminin, fibronectin) in different group at day14. NS, normal saline; αPD-1, anti-PD-1 antibody; αPD-1/Gal, anti-PD-1 antibody and TGF-β receptor I inhibitor galunisertib; GPNP, gelatinase-responsive nanoparticles

effects. Upregulation of Ly6C was also observed in CD8⁺T lymphocytes (Fig. S6, Table S3) in the TME of the GPNP group. Ly6C expression was marked as a memory marker correlated with CD8⁺ T cells IFN γ production after stimulation [20]. However, the role of PD-1 expression in activated Ly6C⁺CD8⁺ T cells remained unclear. Notably, PD-L1⁺CD38⁺CD206⁺ M2 macrophages and PD-1⁺CD38⁺MHCII^{-/low}CD206⁺ M2 macrophages were nearly absent in GPNP group (Fig. S6, Table S3). PD-L1 was mainly expressed on M2 macrophages and its overexpression was proved to suppress tumor infiltrating CD8⁺ T cell function [21]. On the other hand, MHCII^{-/low} macrophages were considered to be functionally impaired since the loss of antigen presenting connection with T cells and their PD-1 expression could be negatively

associated with phagocytic potency against tumor cells [22]. Accordingly, our result highlights the quiescence of the immunosuppressive PD-L1⁺CD38⁺CD206⁺ M2 and PD-1⁺CD38⁺MHCII^{-/low}CD206⁺ M2 subsets might be the key to conquer “cold tumor” status.

To deepen our understanding of TME alterations, we conducted RNAseq analysis, revealing insights into both immune response and ECM dynamics within the GPNP-treated cohort. The immune-related differentially expressed genes were predominantly enriched in cytokines and macrophage reprogramming within the tumor microenvironment. *Ccl21d*-encoded CCL21 protein, secreted by invasive tumors, was described to be involved in promoting tumor immune evasion by creating a tolerant stromal microenvironment [23]. *Ccl21* was

also known to be a secondary lymphoid chemokine that attracted leucocytes except Tregs [24] while *Ccl11* was reported to attract Tregs and promote epithelial-mesenchymal transition (EMT), which might provide a clue to the difference in Treg percentage of α PD-1/Gal group and GPNP group in TME [25, 26]. *Cxcl5*, *Cxcl2*, *Cxcl12* were known to direct and activate migration of immune cells in solid tumors, including neutrophils and CD8⁺ T cells and *Slc7a2* and *Il1rn* worked as the upstream strain of those CXC chemokines [27], demonstrating that not only CD8⁺ T cells but neutrophils might hold great importance in enhancing GPNP therapeutic efficacy. *Sfrp2* could promote M1 polarization as well as macrophage migration [28]. *Slc7a2* and *Fbln7* could prevent M2 activation and differentiation [29, 30]. *Cdh11*, on the other hand, could prevent impaired monocyte-to-macrophage differentiation and phagocytic function [31]. In all, higher expression of *Sfrp2*, *Slc7a2*, *Cdh11* and *Fbln7* in GPNP group secured macrophage production, promoted a shift to M1 and prevented M2 activation, which was consistent with our cytometry results with higher percentage of M1 and relatively lower percentage of M2. For ECM dynamics, in GPNP group, we discovered a highly expressed gene *Pmepa1* that could sequester TGF- β signaling downstream Smad proteins from active participation, suggesting that our GPNP might have a better efficiency in TGF- β inhibitor delivery (Fig. 5B) [32]. *Sfrp2* and *Cdh11* were both engaged in TGF- β -induced fibroblast-to-myfibroblast transition (FMT). *MMP12* took part in macrophage-to-myfibroblast transition (MMT) and was correlated with suppression of lung cancer growth, angiogenesis and metastasis [33–35]. Myfibroblasts were the main source of collagen in ECM, which were derived from fibroblasts or contributed by macrophages. *Ctsk* and *MMP12* encoded a collagenolytic lysosomal cysteine protease and macrophage-secreted matrix metalloprotease, respectively [36, 37]. Both genes were of importance for collagen degradation. Interestingly, we also found upregulation of a serial of fibrillary collagen genes (*Col1a1*, *Col1a2*, *Col12a1*, *Col3a1*, *Col5a2*) in GPNP group.

As for GO enrichment analysis, Wnt signaling was proved to be required for TGF- β -mediated fibrosis [38]. As we looked into the genes (*COL1A1*, *SFRP1*, *SFRP2*, *PTK7*) enriched in this term, we found that all 4 genes were significantly upregulated in GPNP group relative to α PD-1/Gal group. *SFRPs* were reported to modulate ECM and suppress tumors by downregulating Wnt signaling [39]. *PTK7* was also proposed as a Wnt signaling inhibitor [40]. The results might be able to serve as a hint for the alteration in ECM and superior GPNP efficacy.

Further results of scRNA-seq revealed more information related to ECM remodeling. And interestingly, IGFbps were reported to associated with drug

sensitization in lung cancer cells [41]. Of note, both GO and Reactome analysis exhibited enrichment in PDGF signaling, a pathway strongly associated with fibroblast activation, proliferation, migration and transition [18]. This inspired us to further investigate with the following fate mapping model.

The subsequent Masson's staining results further corroborated the findings from RNA and scRNA sequencing, indicating that GPNPs exerted a stimulatory effect on immune cell infiltration by modulating the collagen barrier. Additionally, fibroblast *pdgfra* was chosen as the target for constructing a tracer mouse model. We observed co-expression of *pdgfra* and vimentin in the α PD-1/Gal group but not in the GPNP group. Vimentin was a type III intermediate filament protein participated in cytoskeleton network formation, which was crucial for cellular invasion and metastasis, especially mesenchymal-origin cells EMT activity. Through binding with phosphorylated ERK and Rho kinase, vimentin could modify actin and initiate MAPK cascades [42]. The phenomenon might indicate nanoparticulate prolonged and sustained release characteristics could better restrict tumor mobility. Besides, *pdgfra* co-localization with laminin and fibronectin were observed, respectively, in α PD-1 group (Fig. 7D). Both laminin and fibronectin were the major adhesive glycoproteins and were reported to induce integrin-dependent tumor cell invasion [43–45], supporting α PD-1 treatment as a potential promotor of invasiveness and migration in immune-resistant tumor.

Considerable attention has been directed towards investigating the efficacy of TGF- β inhibition in the context of cancer PD-1/PD-L1 immunotherapy, yielding promising outcomes [6, 7, 10, 46–56]. For instance, Castiglioni et al. elucidated that concurrent blockade of TGF- β and PD-L1 facilitates the expansion and differentiation of stem cell-like CD8 T cells, thereby sustaining treatment efficacy [46]. However, this study predominantly focuses on immune cells, overlooking the intricate interplay between immune cells and the TME. Moreover, the requirement for oral administration of insoluble TGF- β inhibition raises concerns regarding drug absorption reliability and prolonged latency attributable to digestive system dynamics. Recent studies by Zhou et al. have demonstrated that targeting mitochondrial metabolism with albumin-based carriers can effectively block the PD-L1 and TGF- β pathways, showing promising potential to enhance tumor sensitivity to radiotherapy and chemotherapy [55, 56]. However, these approaches often lack a deeper investigation into transcriptomic alterations within the tumor microenvironment, which could provide additional insights into the molecular mechanisms underlying treatment response. Additional challenges, such as unintended systemic side effects, underscore the necessity for safer and more efficient delivery methods,

coupled with a deeper comprehension of the underlying mechanisms. Our study not only delves into immune profiles but also elucidates alterations in transcriptomic signatures within the TME. Furthermore, we investigate the transition of fibroblasts, pivotal contributors to collagen, a primary component of the TME and critical contributor of immunotherapeutic resistance [15]. Leveraging our gelatinase-stimuli nanoparticles, we effectively demonstrate heightened efficacy without observable off-target toxicity.

We acknowledge the presence of both biological and technical limitations in this study. Firstly, the sample size in each group is relatively small due to ethical considerations aimed at minimizing animal sacrifice, which may introduce bias. Secondly, while preclinical models are invaluable tools, they may not entirely reflect the complexity of clinical scenarios. In an effort to mitigate this limitation, we employed CIK cells and A549-harboring lung cancer model in this study, aiming to emulate the clinical setting as closely as possible. Thirdly, it's important to note that our immune profiling data may not encompass all immune cell types, and our transcriptomic profiling may not be exhaustive due to technical constraints. To address this, we employed cyTOF and scRNA sequencing methodologies to maximize our exploratory capabilities. Hence, it is evident that further studies are warranted to overcome these limitations and provide a more comprehensive understanding of the subject matter.

In conclusion, this study supports the role of gelatinase-stimulated nanoparticles in enhancing the synergy of TGF- β and PD-1 inhibition. It also reveals changes in immune profiles and transcriptomic signatures within the TME, thereby providing insights into the underlying mechanisms. We believe this study presents a viable strategy for effectively integrating tumor immunotherapy with nanotechnology.

Materials and methods

Chemical and reagents

N-hydroxysuccinimide functionalized methoxypolyethyleneglycol (mPEG-NHS, PEG average Mn 5,000) and polycaprolactone-amine (PCL-NH₂, PCL average Mn 10,000) were purchased from Ruixi biological Technology (Xian, China). Dichloromethane (DCM) and polyvinyl alcohol (PVA) were purchased from Macklin (Shanghai, China). Peptide PVGLIG was obtained from ChinaPeptides (Shanghai, China). Mouse (clone: RMP1-14) and human anti-programmed death-1 monoclonal antibody (α PD-1) were purchased from Bio X Cell (USA) and Innovent Biologics (Jiangsu, China), respectively. Galunisertib (Gal, TGF- β receptor I inhibitor) was purchased from TargetMol Chemicals (USA). DiR iodide was purchased from Bridgen (Beijing, China).

Cell lines

Mouse Lewis lung carcinoma (LLC) cell line, human A549 lung adenocarcinoma cell line and human NCI-H1299 lung adenocarcinoma were purchased from the Cell Bank of Shanghai Institute of Biochemistry and Cell Biology and were cultured in Dulbecco's Modified Eagle's Medium (DMEM, Basalmedia, Shanghai, China containing 10% fetal bovine serum (FBS, Lonsera, Shanghai, China) and 100U ml⁻¹ penicillin/streptomycin (Beyotime Biotechnology, China). All cells were incubated at 37°C with 5% CO₂ humidified atmosphere.

Fabrication and characterization

The mPEG-PVGLIG-PCL copolymer was synthesized via ring-open polymerization and twice amidation as previously described [13] and validated by proton nuclear magnetic resonance spectroscopy (1H NMR, Bruker, Germany). Galunisertib and α PD-1 were loaded on the carriers by double emulsion, referring as GPNPs. Briefly, 5 mg copolymer and 1 mg Gal were first dissolved in 0.5 ml DCM. After adding α PD-1, the mixture was emulsified immediately by sonication with Microson XL2000 (Misonix, USA) in 1.5 ml 5% PVA (w/v) solution, followed by secondary emulsification in 4 ml 1.5% PVA (w/v) solution. The resultant was gently stirred at room temperature to remove organic solvent. Hydrodynamic size and zeta potential of GPNPs were measured by dynamic light scattering (DLS) using Zetasizer Nano ZS90 (Malvern Instruments, UK). The morphology of the particle was visualized by transmission electron microscope (TEM, Model Tecnai 12, Philips, Holland). Drug loading and encapsulation were testified by Micro BCA protein assay kit (Thermo Scientific, USA) and 1200 series HPLC (Agilent Technologies, USA) (column: Agilent Eclipse XDB-C18, 4.6 mm*150 mm, 5 μ m; column temperature 40°C; flow rate: 1.5 mL/min; mobile phase: water: ACN 70:30; injection volume: 6 μ l). 1 mL of GPNPs were sealed in dialysis bag (14,000Da) and immersed in pH 7.0 PBS at 37°C. At predetermined time points, the media was drawn out and replaced with the same volume of PBS. The amount of drug release was examined by HPLC and BCA protein assay kit. Particle physio-stability was observed by measuring the hydrodynamic diameter and surface charge every 3 days. Particles were stored at 4°C before use and the experiment was replicated at least 3 times and averaged.

Cytotoxicity

The cytotoxicity was evaluated by CCK-8 Cell Counting Kit (Vazyme, Jiangsu, China) according to the manufacturer's instructions. Briefly, LLC and H1299 cells were seeded in the 96-well plates at a density of 5×10^3 cells per well and incubated at 37°C. Upon fully attached, the cells were incubated with fresh medium containing

different concentration of GPNPs at 37°C for another 24–48 h. Then, the absorbance at 450 nm was measured after adding 10 µl CCK-8.

Isolation and preparation of CIKs

Blood collection was carried out in accordance with the guidelines verified and approved by the Ethics Committee of Drum Tower Hospital (2021-027-02). All patients provided informed consent. Peripheral blood mononuclear cells (PBMCs) were isolated from healthy donor using Ficoll density gradient and suspended in AIM-V (Gibico, USA). Non-adherent lymphocytes were collected 2 h later and cultured with AIM-V containing 10% fetal bovine serum (FBS, Gibico, USA), 100 ng/ml OKT-3 (eBioscience, USA), 300U/ml rhIL-2 (PeproTech, USA) and 10ng/ml rhIL-15 (PeproTech, USA). The medium was replaced by fresh AIM-V + 10% FBS containing 300 U/ml IL-2 and 10ng/ml IL-15 every 2–3 days.

Killing assay

Human H1299 or murine LLC cells were stained with CFSE for 10 min and incubated in 37°C avoid lights. Then CIK cells expanded from human PBMCs or splenocytes of treated mice were incubated with CFSE-labeled tumor cells at an effector-to-target ratio (E: T) of 10:1 and 20:1 in drug-containing medium at 37 °C for 24 h. Cells were collected and stained with PI at 4 °C in darkness for 20 min 6 h later. After washing for twice, the cells were suspended in FACS buffer before flow cytometry analysis with BD Accuri C6 (BD Biosciences, USA). Flow cytometry analysis was performed using FlowJo V10.

IFN γ secretion

The detection of IFN γ was accomplished by using BD™ Cytometric Bead Array (CBA) Human IFN γ Kit (BD Biosciences, USA) following the manufacturer's instructions. Briefly, 10⁵ H1299 cells were incubated with medium containing 10⁶ CIKs and different formulations of drugs for 24 h and the supernatant was analyzed with BD Accuri C6 (BD Biosciences, USA). Flow cytometry analysis was performed using FlowJo V10.

Animal experiments

6-to-8-week-old female C57BL/6, BALB/c nude mice and *Pdgfra*-Cre and Rosa26-CAG-LSL-tdTomato with C57BL/6 background were obtained from GemPharmatech (Nanjing, China). All animal experiments in this study were approved by the Ethics Committee of Drum Tower Hospital and the procedures were carried out in compliance with guidelines by the Ethics Committee of the Affiliated Drum Tower Hospital of Nanjing University Medical School (2023AE01083). Efforts were made to minimize animal suffering.

Lewis lung carcinoma syngeneic model

C57BL/6 mice were injected subcutaneously with 5 × 10⁶ LLC cells. Tumor sizes were monitored with a digital caliper every 2 to 3 days. The model was established when tumor volume reached ~ 100 mm³.

$$\text{Tumor volume} = \frac{\text{length} \times \text{width}^2}{2}$$

Biodistribution

Particles were loaded with DiR by double emulsion. Following collection by centrifugation, DiR-labeled nanoparticles were washed and suspended with saline before injected into murine model intraperitoneally or intravenously. The mice were anesthetized and scanned (excitation/emission = 740/780) at different time intervals with IVIS Lumina III System (PerkinElmer, USA). Major organs (spleen, kidney, liver, lung, and heart) were harvested for imaging after sacrifice under anesthesia.

Therapeutic efficacy

LLC-bearing C57BL/6 mice were randomized into 4 groups treating with different regimens for 2 weeks: saline group, α PD-1 group (10 mg/kg, once a week), α PD-1/Gal group (10 mg/kg α PD-1, once a week; 50 mg/kg Gal, thrice a week), GPNP group (dose equivalent to 10 mg/kg α PD-1 and 150 mg/kg Gal, once a week). Tumor volumes was recorded every 2 to 3 days and the survival time was observed.

Toxicities

The weights of the mice from different group were observed every 2 to 3 days. Major organs of the mice treated with different regimens were harvested and fixed in 4% paraformaldehyde (PFA). The tissues were routinely embedded with paraffin and sectioned with microtome (Leica Biosystems, Germany). The slices were stained with hematoxylin and eosin (H&E) and observed with microscope.

Reseeding assay

Tumors after being treated with saline or GPNPs were excised and cut into ~ 3 mm × 3 mm × 3 mm sizes and placed in the petri dish. Healthy mice were anesthetized and embedded subcutaneously with prepared tumor pieces. Tumorigenesis and tumor growth were observed.

A549 cell-derived xenograft (CDX) model

BALB/c nude mice were randomized and injected subcutaneously with 10⁷ A549 cells. Tumor sizes were monitored with a digital caliper every 2 to 3 days. The model was established when tumor volume reached ~ 100 mm³.

Adoptive cell transfer

CDX models were randomized into 5 groups treating with different regimens: saline group, CIK group (10^7 CIK cells.), CIK cells (10^7 CIK cells.) + α PD-1 group (200 μ g, once a week), CIK cells (10^7 CIK cells.) + α PD-1 + Gal group (10 mg/kg α PD-1 and 150 mg/kg Gal, once a week), CIK cells (10^7 CIK cells.) + GPNP group (dose equivalent to 10 mg/kg α PD-1 and 150 mg/kg Gal, once a week). 40,000 U human recombinant IL-2 were given intraperitoneally thrice a week for 2 consecutive weeks after T cells transfer. Tumor volumes were recorded every 2 to 3 days and the survival time was observed.

Tumor harvest

Established LLC tumors were excised from mice, minced and digested with 1 mg/ml type IV collagenase (Gibco, USA) in RMPI 1640 using gentleMACS Dissociator (Miltenyi Biotec, Germany). After incubated at 37°C with frequent agitation for 1 h, cells were lysed with ACK lysis buffer (Biosharp, Anhui, China) for removing red blood cells and washed thrice. Single-cell suspension was obtained after filtration through 70- μ m nylon cell strainers.

Immune profiling

For mass cytometry, cells were incubated with 0.25nM 194Pt (Fluidigm) for 5 min on ice to discriminate dead cells before stained with blocking solution and surface antibody cocktail (Table S2). After fixation and permeation with 250nM Ir overnight, cells were stained with intracellular antibodies (Table S2). Cells were rinsed and subsequently analyzed with Fluidigm Helios CyTOF (USA). For flow cytometry, cells were stained with Zombie NIR Viability dye (Biolegend, USA) to distinguish dead cells and stained with indicated antibodies (Table S2) for 30 min on ice in darkness. Cytofix/Cytoperm Fixation and Permeabilization Kit (BD Biosciences, USA) was adopted for CD206 staining. Cells were then rinsed and analyzed with BD FACS Aria III (BD Biosciences, USA). Flow cytometry analysis was performed using FlowJo V10.

Masson's trichrome stain

The study of connective tissue, muscle and collagen fibers was performed using Masson's Trichrome Stain Kit (Solarbio, Beijing, China) according to the manufacturer's protocol. Upon completion of staining, the slides were dehydrated, coverslipped and observed under microscope.

Fate mapping

Mice (C57BL/6 background) carrying Cre recombinase under *Pdgfra* (*Tg(Pdgfra-cre)1Clc/f*) promoters (Jackson Laboratory, USA) were crossed with

tdTomato^{flox} (*Rosa26tm1Cin(CAG-LSL-Cas9-tdTomato)/Gpt*) reporter mice (GemPharmatech, Jiangsu, China). LLC-bearing syngeneic models were established, and mice were randomized into 4 groups with different regimens for 2 weeks: saline group, α PD-1 group (200 μ g, once a week), α PD-1+Gal group (200 μ g α PD-1, once a week; 50 mg/kg Gal, thrice a week), GPNP group (dose equivalent to 200 μ g α PD-1 and 150 mg/kg Gal, once a week). Tumors and major organs were resected from the mice and immediately frozen in optimal cutting medium (O.C.T.). Sections were cut by cryotome (Thermo Scientific, USA). After washing with PBS, the specimens blocked with 5% BSA and permeabilized with Triton X-100. The slices were stained with primary antibody at 4°C overnight followed by incubation with secondary antibody in the dark for 1 h. The sections were then counter-stained with DAPI before mounting with coverslip. The fluorescence was observed via LSM710 laser scanning confocal microscopy (Leica, Germany).

mRNA sequencing

Total RNA was extracted from the sample by TRIzol Reagent (Invitrogen) and RNeasy Mini Kit (Qiagen). After quantification and qualification by Qubit (Invitrogen), spectrophotometer, Agilent 2100 Bioanalyzer (Agilent Technologies, USA) and agarose gels. 2 μ g total RNA per sample with RIN value above 6 was used for library construction. Sequencing libraries were generated using VAHTS mRNA seq v2 Library Prep Kit for Illumina following manufacturer's instructions. Briefly, mRNA was purified by poly T oligo attached magnetic beads and fragmented using fragmentation buffer. First strand cDNA was synthesized followed by the second. After repairing cDNA ends, adding adenylated tails and ligate adapters, the samples were amplified by PCR. Using Qubit HS quantification, Agilent 2100 Bioanalyzer/Fragment Analyzer 5300 for quality control, the libraries were construct with the size around 350 bp and were sequenced on Illumina NovaSeq platform according to the manufacturer's instructions. Differential expression analysis was performed by DESeq2 package. Differentially expressed genes were identified with absolute fold change ≥ 2 and false discovery rate < 0.05 .

Single-cell RNA sequencing (scRNAseq)

Libraries were prepared by SeekOne Digital Droplet Single Cell 3' library preparation kit (SeekGene, Beijing, China) followed by the manufacturer's instructions. Briefly, cells were mixed with reverse transcription reagents before adding to the sample well of SeekOne DD Chip S3. Barcoded hydrogel beads (BHBs) and partitioning oil were dispensed into corresponding wells in Chip S3. After emulsion droplet was formed, reverse transcription was accomplished at 42°C for 90 min followed

by inactivation at 80°C for 15 min. The resulting cDNA was purified from broken droplet and amplified by PCR reaction and then modified (washed, fragmented, end repaired, A-tailed) before ligated to sequencing adaptor. Index PCR was performed to amplify DNA containing cell barcode and unique molecular index (UMI). The final indexed sequencing libraries were quantified and sequenced by Illumina NovaSeq 6000 with PE150 read length or DNBSEQ-T7 platform with PE100 read length. Genes were clustered and analyzed using Seurat package. Cellular identification was performed by SingleR package.

GO, KEGG and reactome enrichment analysis

Enrichment assay was performed by clusterProfiler. Padjust < 0.05, > 1 and false discovery rate (FDR) < 0.05 were adopted for clustering during functional annotation.

Protein-protein network construction

Upregulated genes were imported into String database with the research species set as *mus musculus*. Protein relationships were obtained, and the interaction network was processed by Cytoscape.

Statistical analysis

SPSS Statistics 23 (IBM, USA) and Graphpad Prism 8.0 (USA) were used for data processing. Similar variances between groups were compared statistically. Data are presented as mean ± deviation (S.D.) unless indicated otherwise. $p < 0.05$ for statistical significance.

Supplementary Information

The online version contains supplementary material available at <https://doi.org/10.1186/s12951-025-03129-z>.

Supplementary Material 1

Acknowledgements

The authors would like to acknowledge that the graphical illustrations were created with BioRender and would like to thank Zhichen Sun, Sensen Zhou, Haiting Chen, Shijie Xu, Yanhong Chu, Yanbing Dong, Chenxi Li, Wei Zhang and Xingyu Luo from Nanjing University, Yueling Yang from Nanjing University of Chinese Medicine, Shanchao Diao from Nanjing University of Science and Technology for their support for this work.

Author contributions

YTY and RL conceived and designed the experiments. YTY, ZZ, and AC performed the experiments. YQ, QL, QW, CL, CW, XQ, JS, FM, LY, and BL assisted in the experiments and data analysis. YTY, ZZ, and YQ prepared the manuscript. RL supervised the project.

Funding

The work was supported by National Natural Science Foundation of China grant 82272852 (RL), National Natural Science Foundation of China grant 81972192 (RL), National Natural Science Foundation of China 82103687 (QW), Science Fund for Distinguished Young Scholars of Jiangsu Province BK20240017 (RL), the 6th "333 Project" of Jiangsu Province grant (2020) 2-020 (RL), Nanjing Medical Science and Technology Development Foundation YKK22086 (FL), Jiangsu Provincial Medical Key Discipline ZDXK202233, and Nanjing Medical Key Laboratory of Oncology.

Data availability

All relevant data were available within the article and supplementary files, or available from the corresponding author upon reasonable request.

Declarations

Ethics approval and consent to participate

All experimental procedures have been approved by the Medical Ethics Committee of the Affiliated Drum Tower Hospital of Nanjing University Medicine School (2021-027-02). All animal experiments were performed in accordance with guidelines set by the Animal Care Committee at Drum Tower Hospital (Nanjing, China).

Competing interests

The authors declare no competing interests.

Received: 26 September 2024 / Accepted: 15 January 2025

Published online: 19 February 2025

References

- Kraehenbuehl L, Weng C-H, Eghbali S, Wolchok JD, Merghoub T. Enhancing immunotherapy in cancer by targeting emerging immunomodulatory pathways. *Nat Reviews Clin Oncol*. 2022;19:37–50. <https://doi.org/10.1038/s41571-021-00552-7>.
- Battle E, Massagué J. Transforming growth Factor- β signaling in immunity and Cancer. *Immunity*. 2019;50:924–40. <https://doi.org/10.1016/j.immuni.2019.03.024>.
- Nixon BG, Gao S, Wang X, Li MO. TGF β control of immune responses in cancer: a holistic immuno-oncology perspective. *Nat Rev Immunol*. 2022. <https://doi.org/10.1038/s41577-022-00796-z>.
- Zhang J, et al. Small-molecule modulators of tumor immune microenvironment. *Bioorg Chem*. 2024;145:107251. <https://doi.org/10.1016/j.bioorg.2024.107251>.
- Zhong G, Zhao Q, Chen Z, Yao T. TGF- β signaling promotes cervical cancer metastasis via CDR1as. *Mol Cancer*. 2023;22:66. <https://doi.org/10.1186/s12943-023-01743-9>.
- Mariathasan S, et al. TGF β attenuates tumour response to PD-L1 blockade by contributing to exclusion of T cells. *Nature*. 2018;554:544–8. <https://doi.org/10.1038/nature25501>.
- Tauriello DVF, et al. TGF β drives immune evasion in genetically reconstituted colon cancer metastasis. *Nature*. 2018;554:538–43. <https://doi.org/10.1038/nature25492>.
- Wang Y, et al. Co-inhibition of the TGF- β pathway and the PD-L1 checkpoint by pH-responsive clustered nanoparticles for pancreatic cancer microenvironment regulation and anti-tumor immunotherapy. *Biomaterials Sci*. 2020;8:5121–32. <https://doi.org/10.1039/D0BM00916D>.
- Strait AA, et al. Distinct immune microenvironment profiles of therapeutic responders emerge in combined TGF β /PD-L1 blockade-treated squamous cell carcinoma. *Commun Biology*. 2021;4:1005. <https://doi.org/10.1038/s42003-021-02522-2>.
- Holmgaard RB, et al. Targeting the TGF β pathway with galunisertib, a TGF β RI small molecule inhibitor, promotes anti-tumor immunity leading to durable, complete responses, as monotherapy and in combination with checkpoint blockade. *J Immunother Cancer*. 2018;6:47. <https://doi.org/10.1186/s40425-018-0356-4>.
- Moslehi JJ, Salem J-E, Sosman JA, Lebrun-Vignes B, Johnson DB. Increased reporting of fatal immune checkpoint inhibitor-associated myocarditis. *Lancet*. 2018;391:933. [https://doi.org/10.1016/S0140-6736\(18\)30533-6](https://doi.org/10.1016/S0140-6736(18)30533-6).
- Stauber AJ, Credille KM, Truex LL, Ehlhardt WJ, Young JK. Nonclinical safety evaluation of a transforming growth factor β receptor I kinase inhibitor in Fischer 344 rats and Beagle Dogs. *J Clin Toxicol*. 2014;4:1–10.
- Li R, et al. Intelligently targeted drug delivery and enhanced antitumor effect by gelatinase-responsive nanoparticles. *PLoS ONE*. 2013;8:e69643. <https://doi.org/10.1371/journal.pone.0069643>.
- Li S, et al. Characterization of neoantigen-specific T cells in cancer resistant to immune checkpoint therapies. *Proc Natl Acad Sci*. 2021;118(e2025570118). <https://doi.org/10.1073/pnas.2025570118>.

15. Peng DH, et al. Collagen promotes anti-PD-1/PD-L1 resistance in cancer through LAIR1-dependent CD8+T cell exhaustion. *Nat Commun.* 2020;11:4520. <https://doi.org/10.1038/s41467-020-18298-8>.
16. Butler A, Hoffman P, Stribert P, Papalexis E, Satija R. Integrating single-cell transcriptomic data across different conditions, technologies, and species. *Nat Biotechnol.* 2018;36:411–20. <https://doi.org/10.1038/nbt.4096>.
17. Sahai E, et al. A framework for advancing our understanding of cancer-associated fibroblasts. *Nat Rev Cancer.* 2020;20:174–86. <https://doi.org/10.1038/s41568-019-0238-1>.
18. Pliukus MV, et al. Fibroblasts: origins, definitions, and functions in health and disease. *Cell.* 2021;184:3852–72. <https://doi.org/10.1016/j.cell.2021.06.024>.
19. Shen Y, et al. PD-1 does not mark tumor-infiltrating CD8+T cell dysfunction in human gastric cancer. *J Immunother Cancer.* 2020;8:e000422. <https://doi.org/10.1136/jitc-2019-000422>.
20. Jergović M, et al. Infection-induced type I interferons critically modulate the homeostasis and function of CD8+ naïve T cells. *Nat Commun.* 2021;12:5303. <https://doi.org/10.1038/s41467-021-25645-w>.
21. Petty AJ, et al. Hedgehog-induced PD-L1 on tumor-associated macrophages is critical for suppression of tumor-infiltrating CD8+T cell function. *JCI Insight.* 2021;6. <https://doi.org/10.1172/jci.insight.146707>.
22. Gordon SR, et al. PD-1 expression by tumour-associated macrophages inhibits phagocytosis and tumour immunity. *Nature.* 2017;545:495–9. <https://doi.org/10.1038/nature22396>.
23. Richmond A. Chemokine modulation of the tumor microenvironment. *Pigment cell Melanoma Res.* 2010;23:312–3. <https://doi.org/10.1111/j.1755-148X.2010.00714.x>.
24. Lin Y, Sharma S, John MS. CCL21 Cancer Immunotherapy. *Cancers (Basel).* 2014;6:1098–110. <https://doi.org/10.3390/cancers6021098>.
25. Wang R, Huang K. CCL11 increases the proportion of CD4+CD25+Foxp3+Treg cells and the production of IL-2 and TGF-β by CD4+T cells via the STAT5 signaling pathway. *Mol Med Rep.* 2020;21:2522–32. <https://doi.org/10.3892/mmr.2020.11049>.
26. Lin S, et al. Myeloid-derived suppressor cells promote lung cancer metastasis by CCL11 to activate ERK and AKT signaling and induce epithelial-mesenchymal transition in tumor cells. *Oncogene.* 2021;40:1476–89. <https://doi.org/10.1038/s41388-020-01605-4>.
27. Kohli K, Pillarisetty VG, Kim TS. Key chemokines direct migration of immune cells in solid tumors. *Cancer Gene Ther.* 2022;29:10–21. <https://doi.org/10.1038/s41417-021-00303-x>.
28. Mei J, Zhou F, Qiao H, Li H, Tang T. Nerve modulation therapy in gouty arthritis: targeting increased sFRP2 expression in dorsal root ganglion regulates macrophage polarization and alleviates endothelial damage. *Theranostics.* 2019;9:3707–22. <https://doi.org/10.7150/thno.33908>.
29. Coburn LA, et al. Loss of solute carrier family 7 member 2 exacerbates inflammation-associated colon tumorigenesis. *Oncogene.* 2019;38:1067–79. <https://doi.org/10.1038/s41388-018-0492-9>.
30. Chakraborty P, et al. A C-terminal fragment of adhesion protein fibulin-7 inhibits growth of murine breast tumor by regulating macrophage reprogramming. *FEBS J.* 2021;288:803–17. <https://doi.org/10.1111/febs.15333>.
31. To S, Chavula T, Pedroza M, Smith J, Agarwal SK. Cadherin-11 regulates macrophage development and function. *Front Immunol.* 2022;13:795337. <https://doi.org/10.3389/fimmu.2022.795337>.
32. Watanabe Y, et al. TMEPAI, a transmembrane TGF-beta-inducible protein, sequesters smad proteins from active participation in TGF-beta signaling. *Mol Cell.* 2010;37:123–34. <https://doi.org/10.1016/j.molcel.2009.10.028>.
33. Houghton AM, et al. Macrophage elastase (matrix metalloproteinase-12) suppresses growth of lung metastases. *Cancer Res.* 2006;66:6149–55. <https://doi.org/10.1158/0008-5472.can-04-0297>.
34. Acuff HB, et al. Analysis of host- and tumor-derived proteinases using a Custom Dual species microarray reveals a protective role for stromal matrix Metalloproteinase-12 in non-small cell Lung Cancer. *Cancer Res.* 2006;66:7968–75. <https://doi.org/10.1158/0008-5472.can-05-4279>.
35. Tabib T, et al. Myofibroblast transcriptome indicates SFRP2hi fibroblast progenitors in systemic sclerosis skin. *Nat Commun.* 2021;12:4384. <https://doi.org/10.1038/s41467-021-24607-6>.
36. Bossard MJ, et al. Proteolytic activity of human osteoclast cathepsin K. expression, purification, activation, and substrate identification. *J Biol Chem.* 1996;271:12517–24. <https://doi.org/10.1074/jbc.271.21.12517>.
37. Yi C, et al. Macrophage elastase (MMP12) critically contributes to the development of subretinal fibrosis. *J Neuroinflamm.* 2022;19. <https://doi.org/10.1186/s12974-022-02433-x>.
38. Akhmetshina A, et al. Activation of canonical wnt signalling is required for TGF-β-mediated fibrosis. *Nat Commun.* 2012;3:735. <https://doi.org/10.1038/ncomms1734>.
39. Liang C-J, et al. SFRPs are biphasic modulators of wnt-signaling-elicited Cancer Stem Cell Properties beyond Extracellular Control. *Cell Rep.* 2019;28:1511–e15251515. <https://doi.org/10.1016/j.celrep.2019.07.023>.
40. Peradziryi H, et al. PTK7/Otk interacts with wnts and inhibits canonical wnt signalling. *EMBO J.* 2011;30:3729–40. <https://doi.org/10.1038/emboj.2011.236>.
41. Remsing Rix LL, et al. IGF-binding proteins secreted by cancer-associated fibroblasts induce context-dependent drug sensitization of lung cancer cells. *Sci Signal.* 2022;15:eabj5879. <https://doi.org/10.1126/scisignal.abj5879>.
42. Pérez-Sala D, et al. Vimentin filament organization and stress sensing depend on its single cysteine residue and zinc binding. *Nat Commun.* 2015;6:7287. <https://doi.org/10.1038/ncomms8287>.
43. Givant-Horwitz V, Davidson B, Reich R. Laminin-Induced Signaling in Tumor cells: the role of the Mr 67,000 laminin receptor. *Cancer Res.* 2004;64:3572–9. <https://doi.org/10.1158/0008-5472.can-03-3424>.
44. Rousselle P, Scoazec JY. Laminin 332 in cancer: when the extracellular matrix turns signals from cell anchorage to cell movement. *Sem Cancer Biol.* 2020;62:149–65. <https://doi.org/10.1016/j.semcancer.2019.09.026>.
45. Attieh Y, et al. Cancer-associated fibroblasts lead tumor invasion through integrin-β3-dependent fibronectin assembly. *J Cell Biol.* 2017;216:3509–20. <https://doi.org/10.1083/jcb.201702033>.
46. Castiglioni A, et al. Combined PD-L1/TGFβ blockade allows expansion and differentiation of stem cell-like CD8 T cells in immune excluded tumors. *Nat Commun.* 2023;14:4703. <https://doi.org/10.1038/s41467-023-40398-4>.
47. Park BV, et al. TGFβ1-Mediated SMAD3 enhances PD-1 expression on Antigen-Specific T cells in Cancer. *Cancer Discov.* 2016;6:1366–81. <https://doi.org/10.1158/2159-8290.cd-15-1347>.
48. de Streef G, et al. Selective inhibition of TGF-β1 produced by GARP-expressing Tregs overcomes resistance to PD-1/PD-L1 blockade in cancer. *Nat Commun.* 2020;11:4545. <https://doi.org/10.1038/s41467-020-17811-3>.
49. Principe DR, et al. TGFβ blockade augments PD-1 inhibition to promote T-Cell-mediated regression of pancreatic Cancer. *Mol Cancer Ther.* 2019;18:613–20. <https://doi.org/10.1158/1535-7163.mct-18-0850>.
50. Terabe M, et al. Blockade of only TGF-β 1 and 2 is sufficient to enhance the efficacy of vaccine and PD-1 checkpoint blockade immunotherapy. *Oncolimmunology.* 2017;6:e1308616. <https://doi.org/10.1080/2162402X.2017.1308616>.
51. Lan Y, Zhang D. Enhanced preclinical antitumor activity of M7824, a bifunctional fusion protein simultaneously targeting PD-L1 and TGF-β. *10*. <https://doi.org/10.1126/scitranslmed.aan5488> (2018).
52. Yi L, et al. A hybrid Nanoadjuvant simultaneously depresses PD-L1/TGF-β1 and activates cGAS-STING pathway to overcome radio-immunotherapy resistance. *Adv Mater.* 2024;36:2304328. <https://doi.org/10.1002/adma.202304328>.
53. Jiang X, et al. Mitochondrial disruption Nanosystem simultaneously depressed programmed death Ligand-1 and transforming growth Factor-β to overcome photodynamic immunotherapy resistance. *ACS Nano.* 2024;18:3331–48. <https://doi.org/10.1021/acsnano.3c10117>.
54. Zhou Z, et al. Mitochondria-targeted nanoadjuvants Induced Multi-functional Immune-Microenvironment remodeling to sensitize Tumor Radio-Immunotherapy. *Adv Sci.* 2024;11:2400297. <https://doi.org/10.1002/adv.202400297>.
55. Zhou Z, et al. Mitochondria Energy Metabolism Depression as Novel adjuvant to sensitize Radiotherapy and inhibit Radiation Induced-Pulmonary Fibrosis. *Adv Sci.* 2024;11:2401394. <https://doi.org/10.1002/adv.202401394>.
56. Zhou Z, et al. Mitochondrial metabolism blockade nanoadjuvant reversed immune-resistance microenvironment to sensitize albumin-bound paclitaxel-based chemo-immunotherapy. *Acta Pharm Sinica B.* 2024;14:4087–101. <https://doi.org/10.1016/j.apsb.2024.05.028>.

Publisher's note

Springer Nature remains neutral with regard to jurisdictional claims in published maps and institutional affiliations.